Computational Study on Finned Reusable Rocket Aerodynamics during Turnover

By Takuya Aogaki,[1] Keiichi Kitamura,[1] and Satoshi Nonaka[2]

[1)]*Graduate School of Engineering, Yokohama National University, Kanagawa, Japan*
[2)]*Institute of Space and Astronautical Science, JAXA, Sagamihara, Japan*

The development of a fully reusable vertical-takeoff-and-vertical-landing (VTVL) rocket is indispensable for reducing space transportation costs. However, there are many technical issues associated with such vehicles, such as turnover maneuvers during return flight where the pitching moment plays a key role. It is known that aerodynamic characteristics can be controlled by installing aerodynamic devices, but the relationship between the aerodynamic characteristics and the flowfields has not been explored. To clarify this relationship using computational fluid dynamics (CFD), we investigated these flowfields and aerodynamic characteristics, in the case where we install such devices (fins) in the nose part of a reusable rocket. We found that vortices form downstream of the aerodynamic devices. For angles of attack between 0 and 90 degrees (in which the fins are located in the upstream portion), these vortices significantly affect the surface pressure on the rocket and increase the pitching moment. On the other hand, for AOAs between 90 to 180 degrees (in which the fins are in the downstream portion), the effect of these vortices on the on-surface pressure is negligible, and only vortices formed near the surface of the fins increase the pitching moment.

Key Words: Reusable Rocket, Fin, High Angle of Attack

Nomenclature

|		
a	:	speed of sound
C_m	:	pitching moment coefficient
C_p	:	pressure coefficient
e_T	:	total energy per unit mass
F_x	:	axial force
F_z	:	normal force
L	:	body length
M	:	Mach number
M_y	:	pitching moment
P	:	static pressure
Pr	:	Prandtl number
q	:	dynamic pressure
Re	:	Reynolds number
$\lvert S \rvert$	:	Euclidean norm of the strain-rate tensor
S_{base}	:	base (reference) area
T	:	temperature
U	:	flow velocity
u, v, w	:	velocity components
x, y, z	:	body-fixed coordinates
δ	:	Kronecker's delta
κ	:	thermal conductivity
μ	:	viscosity
ρ	:	density
τ	:	stress tensor
$\lvert \Omega \rvert$	:	Euclidean norm of the vorticity tensor
Subscripts		
∞	:	freestream value
i	:	value at a cell
t	:	turbulent

1. Introduction
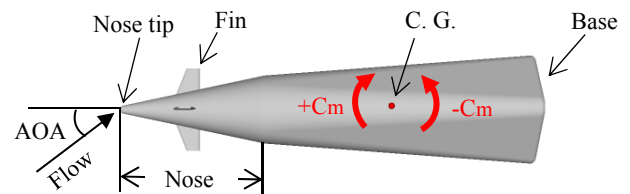
Fig. 1.   Reusable rocket configuration and definitions of terms.

A reusable VTVL rocket vehicle has been proposed by ISAS/JAXA as a future space transportation system.[1] This rocket enables us to reduce space transportation costs significantly, because it is intended to be reused more than 100 times. However, there are many technical issues associated with the development of this rocket, such as how to land the rocket safely. To resolve this problem, analysis of the return flight phase is crucial. The reusable rocket configuration and definitions of terms used in this paper are shown in Fig. 1.

Figure 2 shows two methods (Nose-Entry and Base-Entry) for the return flight of a reusable rocket. A previous study[2] concluded that the Nose-Entry is more suitable for this reusable rocket because a larger lift-to-drag ratio can be achieved with a relatively slender shape (thereby reducing the drag during launch) by using Nose-Entry. For this reason, we adopted Nose-Entry as the return flight method in this study.

In case of Nose-Entry, a turnover maneuver is conducted during the return flight. This maneuver is conducted to change the attitude of the vehicle from the nose-first to the base-first by using the aerodynamic force (pitching moment) acting on the vehicle. This enables the vehicle to decelerate and achieve

a soft landing. A pitching moment characteristic of a slender body vehicle during the turnover[3] is shown in Fig. 3. The pitching moment is positive for AOAs between 0 and 90 degrees (designated as "Forward" AOA hereafter). Therefore, a nose-up moment acts on the vehicle in this AOA region, and the angular velocity of the vehicle is increased. On the other hand, the pitching moment is negative from for AOAs between 90 and 180 degrees ("Backward" AOA). Therefore, a nose-down moment acts on the vehicle in this region, and the angular velocity of the vehicle is decreased. If the area of the nose-up moment ("Area1" in Fig. 3) and that of the nose-down moment ("Area2" in Fig. 3) are nearly equal, the positive and negative angular accelerations cancel each other out, and a quasi-stable state can be realized at AOA = 180 degrees.[4] Thus, an understanding of pitching moment characteristics of slender bodies at AOAs between 0 and 180 degrees is important in accomplishing the turnover.

Many studies were carried out to explore the aerodynamic characteristics of a reusable rocket. Shimojima[5] and Kinami[6] found experimentally that the area of the nose-up moment can be made almost identical to that of the nose-down moment by using a body configuration which has a square-like cross-section. Aogaki et al.[7] numerically investigated the aerodynamics of a reusable rocket in detail, including the surrounding flowfields, and clarified that wakes of such vehicles greatly affect their aerodynamic characteristics. Okamoto[3] and Nakamura[8] installed aerodynamic devices on the vehicle (Fig. 1) and obtained aerodynamic coefficients from wind-tunnel tests. They[3,8] showed that the aerodynamic characteristics of a reusable rocket can be controlled by installing aerodynamic devices. However, the relationship between the flowfields and the aerodynamic characteristics is not well understood as it is difficult to visualize detailed flowfields in experiments. In this study, acquisition of aerodynamic characteristics and flow visualization are conducted using CFD to investigate the above-mentioned relationship.
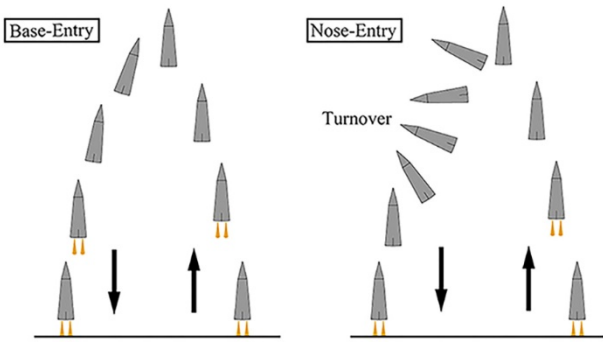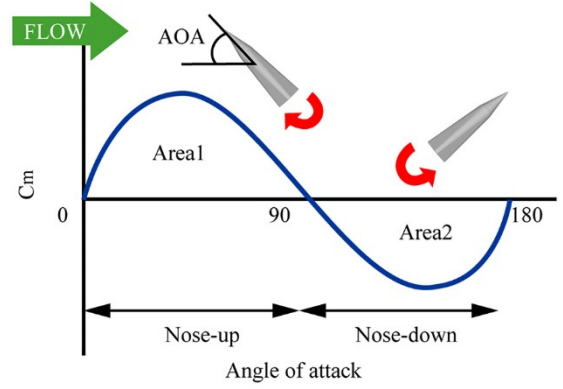

Fig. 2.   Flight profile.

Fig. 3.   Pitching moment characteristic of a slender body.

2.   Numerical Setup

2.1.   Configuration

The reusable rocket configuration we used is shown in Fig. 4. As depicted in Fig. 4, we installed fins in the nose part of the vehicle. Here, four fins were installed at 90-degree increments in the circumferential direction. The positions of fins were established such that the main stream directly impinges on the fins. Thus, the fins have an effect on aerodynamic moment control.[3] The baseline configuration (without fins) of this vehicle is identical to that of previous studies.[5)-7)] The dimensions in Fig. 4 are in "mm".

(a)   Entire vehicle   (b)   Fin
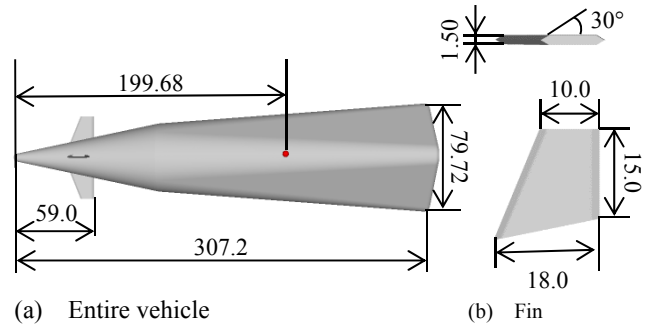Fig. 4.   Reusable rocket configuration (mm).

2.2.   Governing equations

The governing equations for the flow are three-dimensional compressible Navier-Stokes equations (Eqs. (1) to (3)).

$$\frac{\partial Q}{\partial t} + \frac{\partial Fe_k}{\partial x_k} = \frac{1}{\mathrm{Re}} \frac{\partial Fv_k}{\partial x_k} \qquad (1)$$

$$Q = \begin{pmatrix} \rho \\ \rho u_l \\ e_T \end{pmatrix} \ , \quad Fe_k = \begin{pmatrix} \rho u_k \\ \rho u_l\, u_k + p\delta_{lk} \\ (e_T + p)u_k \end{pmatrix} \ ,$$

$$Fv_k = \begin{pmatrix} 0 \\ \tau_{lk} \\ u_m \tau_{mk} + \dfrac{\kappa}{(\gamma - 1)\mathrm{Pr}} \dfrac{\partial T}{\partial x_k} \end{pmatrix} \qquad (2)$$

$$\tau_{lk} = \mu \left(\frac{\partial u_l}{\partial x_k} + \frac{\partial u_k}{\partial x_l} \right) - \frac{2}{3} \mu \frac{\partial u_n}{\partial x_n} \delta_{lk} \qquad (3)$$

where subscripts k, l, m, and n take the values 1, 2 and 3 denoting the body-fixed coordinates. All quantities are dimensionless. The working gas is air approximated by the calorically perfect gas model with a specific heat ratio of $\gamma = 1.4$. The molecular viscosity μ is calculated using Sutherland's law. The thermal conductivity κ is obtained from $\kappa = \mu$, assuming that Prandtl number is constant, with $Pr = 0.71$. For modeling turbulence, the molecular viscosity is replaced by $(\mu + \mu_t)$, where μ_t is the turbulent viscosity given by the turbulence model. Similarly, the thermal conductivity κ is replaced by $(\mu + \mu_t Pr/Pr_t)$, where the turbulent Prandtl number is $Pr_t = 0.90$. The Reynolds number is defined as shown in Eq. (4).

$$Re = \frac{\rho_\infty U_\infty L}{\mu_\infty} \frac{a_\infty}{U_\infty} = \frac{Re_\infty}{M_\infty} \qquad (4)$$

2.3. Computational methods

We used FaSTAR[9] a high-speed flow solver developed at JAXA, for calculations. The system of equations (Eqs. (1) to (3)) was discretized and solved by cell-vertex finite volume method for unstructured grids with second-order accuracy in both space and time. We employed DDES[10] as the turbulence model to capture the wake accurately. A numerical flux of the inviscid term was calculated from an AUSM type scheme, SLAU.[11] The GLSQ method[12] was used for the gradient calculations within the MUSCL[13] framework along with the Venkatakrishnan limiter.[14] For time integration, preconditioned LU-SGS[15] was adopted with dual-time-stepping, and unsteady simulations were conducted. Here, the time step was set to $dt \approx 8.8 \times 10^{-6}$ s and the total number of time steps was set to 30000.

2.4. Computational grids

We used MEGG3D[16] an automatic meshing tool developed at JAXA, to generate the computational grid shown in Fig. 5. As shown in Fig. 5, the coordinate system was defined such that the X-axis was along the axial direction of the vehicle, the Y-axis was the axis around which the pitch moment was defined, and the Z-axis was orthogonal to these two. In addition, the number of nodes (and hence, elements) was approximately 28.70 million. We set the first cell height so that $y^+ < 0.1$, with the aim of predicting the boundary layer at the nose as accurately as possible, with reasonable computational cost.
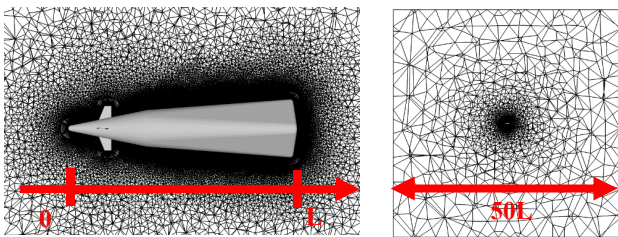
(a) Body   (b) Overview
Fig. 5. Computational grid.

2.5. Computational conditions

The computational conditions were selected to correspond to wind-tunnel tests.[3,8] The freestream flow velocity U_∞ was set to 30 m/s (Mach number $M_\infty = 0.08643$). The freestream Reynolds number based on the body length L was $Re_\infty = 6.0 \times 10^5$. Moreover, the center of gravity was set to 65 percent of the body length from the nose tip.

For convenience, we classified the computational cases according to AOA as shown in Table 1. We calculated 6 cases in total; 3 cases for AOAs less than 90 degrees and 3 cases for AOAs greater than 90 degrees.

Table 1. Computational cases.

Case	AOA [degrees]
Forward angles	20, 40, 60
Backward angles	130, 150, 170

2.6. Aerodynamic coefficients

The pitching moment coefficient is defined as follows.

$$C_m = \frac{M_y}{q_\infty S_{base} L} \qquad (5)$$

The pitching moment M_y is determined from $\sum_i \{F_{zi}(x_G - x_i) - F_{xi}(z_G - z_i)\}$, where x_G and z_G are the X and Z coordinates of the center of gravity, respectively. F_{xi} and F_{zi} are calculated from pressure and friction forces.

3. Results and Discussion

In this section, we discuss the results acquired from CFD simulations. All figures show time-averaged results. For the time-averaging process, data were obtained every 100 steps, from step 10100 to step 30000, yielding a total of 200 data points. These values were established such that this process includes at least ten cycles, and each cycle includes at least ten instantaneous values. Here, a cycle was defined as the main period of the C_m hysteresis calculated using a Fast Fourier Transform.

3.1. Validation

Figure 6 shows the pitching moment coefficients obtained from our simulations along with experimental results.[8]
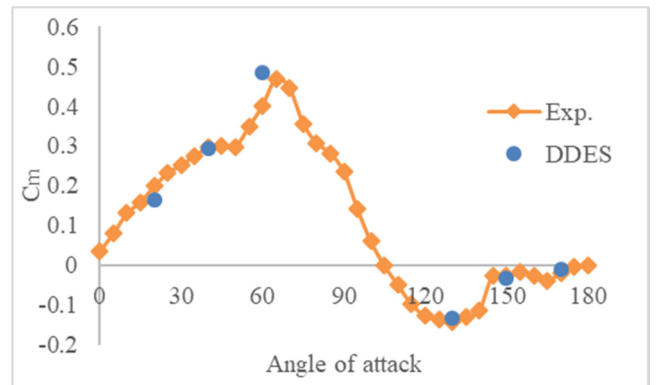

Fig. 6. Pitching moment coefficients.

Based on Fig. 6, it can be seen that the pitching moment coefficients of our simulations are in good agreement with those of the reference experiment, although there is a slight deviation from the experimental results at 60 degrees. Nevertheless, this deviation is not large. We regard our calculations as valid and use these results for discussion.

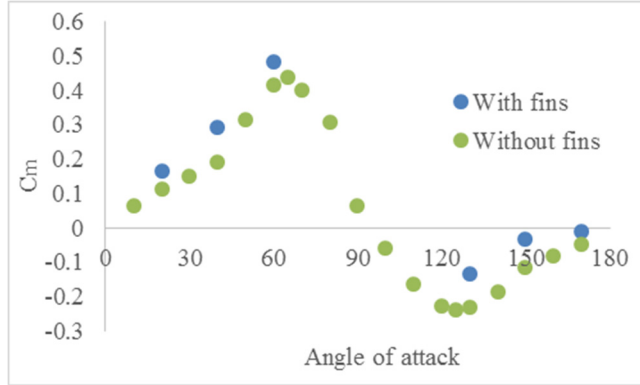## 3.2. Effects of fins: Pitching moment coefficients

Fig. 7. Comparison of pitching moment coefficients.

Figure 7 shows the pitching moment coefficients of the configuration both with and without fins.[7] Both results are obtained by DDES (details of the computational methods, grid, and so forth for the configuration without fins can be found in Ref. 7). As shown in Fig. 7, the pitching moment coefficients can be increased by installing fins at all six AOAs; this effect was also described in the experimental study in Ref. 8). To investigate this phenomenon in detail, we will visualize the flowfields in the next section.

3.3. Effects of fins: Flowfields

3.3.1. Forward angles

First, we will discuss the results at an AOA of 20 degrees. Figure 8 shows the isosurface of the second invariants of the velocity vector tensor (Q) colored with the pressure coefficient ($Q = 5 \times 10^{-7}$). Here, Q is obtained from $Q = (|\Omega|^2 - |S|^2)/2$, and velocity component used in this equation is nondimensionalized using the freestream speed of sound. From Fig. 8, we can observe the difference in the formation of vortices between two configurations. In Fig. 8 (a), a pair of vortices (FV) is generated from the downstream side of the fins, whereas in Fig. 8 (b), vortices (V1) are generated from the nose. We postulate, in the case with fins, that vortices are firstly developed from the nose, but these are entrained in the flow near the fins. As a result, the vortices are not developed until the flow passes through the fins. The difference of flowfields arises due to this. In addition, vortices cause the reduction in pressure on the leeward side of the fins as shown in Fig. 8 (a). To investigate the effect of these differences on the pitching moment coefficient, the on-surface pressure distribution is shown in Fig. 9. Comparing Figs. 9 (a) and (b), it can be seen that the notable differences of the pressure distributions arise near the fins. Moreover, the pressure difference is larger near the fins than that near the base, and therefore, we postulate that the pressure reduction on the downstream side of fins and the pressure increase on the upstream side causes the increase in pitching moment coefficient ($C_m = 0.16$; 45 % increase) in

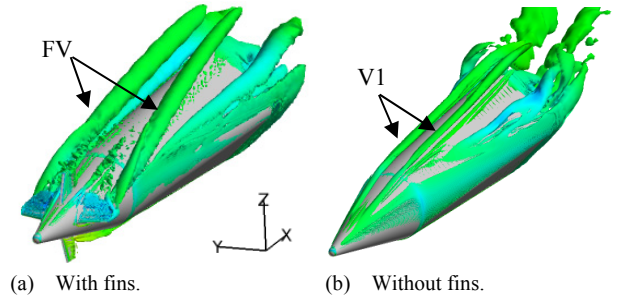comparison to the configuration without fins ($C_m = 0.11$).

(a)   With fins.   (b)   Without fins.

Fig. 8. Q isosurface colored with C_P (AOA=20 degrees).

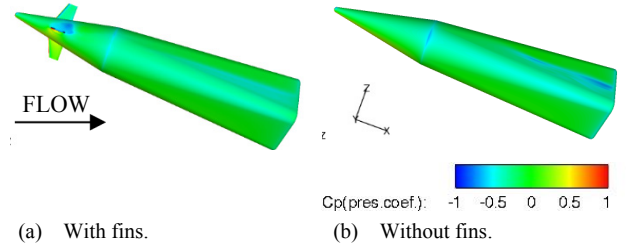(a)   With fins.   (b)   Without fins.

Fig. 9.   Pressure distribution (AOA=20 degrees).

As with the cases with an AOA of 20 degrees, the Q isosurface ($Q = 5 \times 10^{-7}$) and the on-surface pressure distribution at 40 degrees are shown in Figs. 10 and 11, respectively. Once again, these figures are colored with the pressure coefficient. By comparing Figs. 10 (a) and (b), it can be seen that the downstream flow is significantly different between two cases. In Fig. 10 (a), fin-vortices (FV) are generated from the downstream side of the fins, but in Fig. 10 (b) vortices (V1) are formed from the nose; this difference was also observed at an AOA of 20 degrees. In the case of the configuration without fins, another pair of vortices (V2) is generated and these vortices are asymmetric, though this asymmetry is suppressed in the case with fins. In Fig. 11, we can see the differences in the pressure distributions, which arise due to the differences in formations of vortices. As with the AOA of 20 degrees case, these differences have an effect on the pitching moment coefficients of these two cases at an AOA of 40 degrees. In particular, we postulate that the pressure difference near the fins contributes to the increase of the pitching moment coefficient in the case with fins (from $C_m = 0.19$ to 0.29; 54 % increase), as pressure distributions near the center of gravity have a negligible effect on pitching moments.
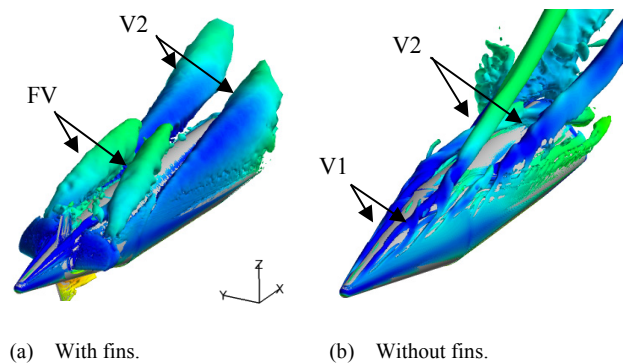

(a)   With fins.   (b)   Without fins.

Fig. 10. Q isosurface colored with C_P (AOA=40 degrees).

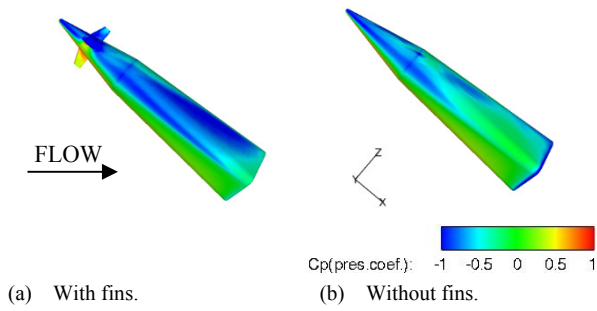(a) With fins.   (b) Without fins.

Fig. 11. Pressure distribution (AOA=40 degrees).

The Q isosurface ($Q = 5 \times 10^{-7}$) and the on-surface pressure distribution for the cases where AOA is 60 degrees is shown in Figs. 12 and 13, respectively. As shown in Fig. 12 (b), in the case without fins, the vortices are generated from the nose (V1), and another pair of vortices (V2) form from $x/L \approx$ 0.39. On the port side, V1 and V2 merge (V1+V2), yet these vortices are not combined on the starboard side. Moreover, V2 and V1+V2 detach from the body near the center of gravity. On the other hand, in the case with fins (Fig. 12 (a)), vortices (FV) are produced from the fins, and V2 are generated from $x/L \approx$ 0.33 on the starboard side and $x/L \approx$ 0.72 on the port side. These vortices do not merge downstream. As shown in Fig. 13, these differences affect the on-surface pressure distributions. The pressure distributions are different near the fins and around the center of gravity. The former increases the pitching moment, whereas the latter has a negligible effect on the pitching moment. As a result, the pitching moment increases also at this AOA (from C_m = 0.41 to 0.48; 17 % increase).
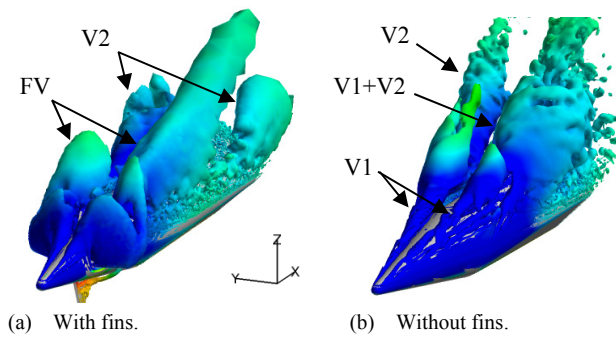

(a) With fins.   (b) Without fins.

Fig. 12. Q isosurface colored with C_P (AOA=60 degrees).

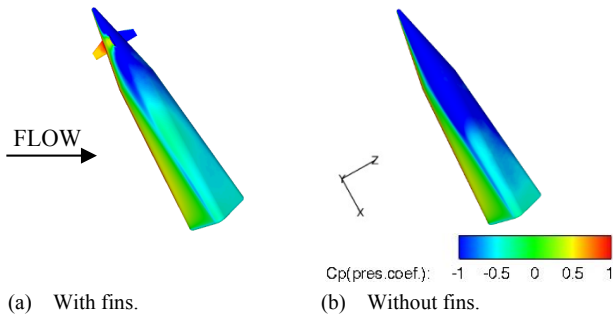(a) With fins.   (b) Without fins.

Fig. 13. Pressure distribution (AOA=60 degrees).

To summarize the results at forward angles: the fins cause the generation of vortices, and because of this, the state of the downstream flow is also affected. This causes the differences in the on-surface pressure distributions (especially on the fins)

between the configurations with and without fins, and results in an increase in the pitching moment coefficients in the cases with fins at all the forward angles.

3.3.2. Backward angles

For the cases where the AOA is 130 degrees, the Q isosurface ($Q = 1 \times 10^{-6}$) is shown in Fig. 14. Here, the viewpoint of isosurface is changed from that of the forward angles to improve visibility of the vortices at backward angles. In Fig. 14, the flowfields are almost identical between two cases. The only difference is that in the case with fins, vortices (FV) are generated downstream of the fins which decrease the local pressure. In order to investigate the effect of these vortices on the pitching moment coefficient, the on-surface pressure distribution is shown in Fig. 15. The difference in the pressure distributions is observed only near the fins. As a consequence, we determined that FV contributes to the increase in the pitching moment coefficient, from C_m = -0.23 to -0.13 (43 % increase).
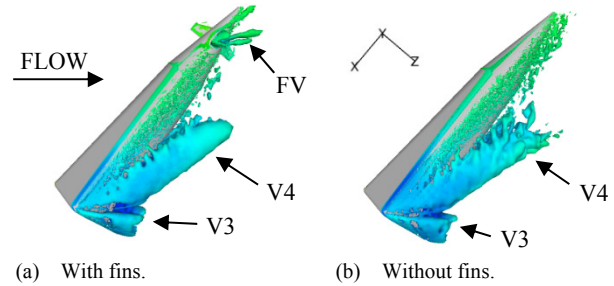

(a) With fins.   (b) Without fins.

Fig. 14. Q isosurface colored with C_P (AOA=130 degrees).
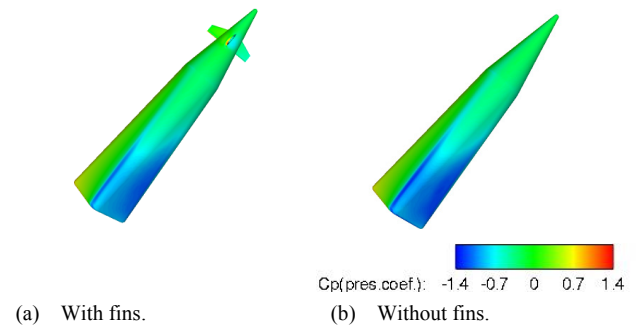

(a) With fins.   (b) Without fins.

Fig. 15. Pressure distribution (AOA=130 degrees).

Figures 16 and 17 show the Q isosurface ($Q = 1 \times 10^{-6}$), and the on-surface pressure distribution for an AOA of 150 degrees, respectively. From Fig. 16, a slight difference in the flowfields between two cases can be seen. As with the cases with an AOA of 130 degrees, the flowfields between the base and the fins are almost the same. The only difference is that vortices (FV) are present on the leeward side of fins (Fig. 16 (a)), whereas no vortices form near the nose in the case without fins (Fig. 16 (b)). From Fig. 17, the difference in the on-surface pressure distribution is also observed only near the fins. From these results, we determined that the fin-vortices cause an increase in the pitching moment coefficient (from C_m = -0.12 to -0.032; 72 % increase).
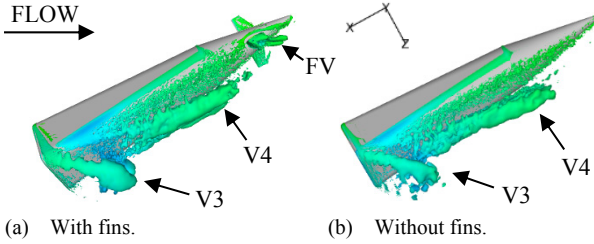
(a) With fins. (b) Without fins.

Fig. 16. Q isosurface colored with C_P (AOA=150 degrees).

Cp(pres.coef.): -1.4 -0.7 0 0.7 1.4
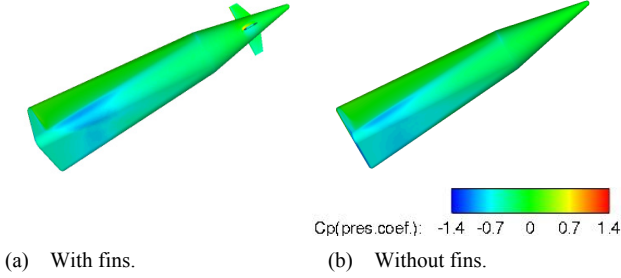
(a) With fins. (b) Without fins.

Fig. 17. Pressure distribution (AOA=150 degrees).

Finally, the results for the cases where the AOA is 170 degrees are discussed. As with the other AOAs, the Q isosurface ($Q = 1 \times 10^{-6}$) and the on-surface pressure distribution are shown in Figs. 18 and 19, respectively. From these figures, it can be seen that the difference between two cases is negligible. From Fig 18 (a), it can be seen that vortices (FV) are generated downstream of the fins once again. However, as shown in Fig. 18 (b), vortices (V5) also form at the nose, and therefore the flowfields of these two cases are similar. In Fig. 19, the difference of pressure distributions is hardly observed. We consider that the difference in the pressure distributions on the body surfaces arises only on the fins (this pressure distribution is not visible in Fig. 19 because these surfaces are perpendicular to the plane of the figure), and because of this, the pitching moment coefficients are almost the identical between these two cases ($C_m \approx -0.048$: without fins and $C_m \approx -0.0092$: with fins, 81% increase), as in Fig. 7.
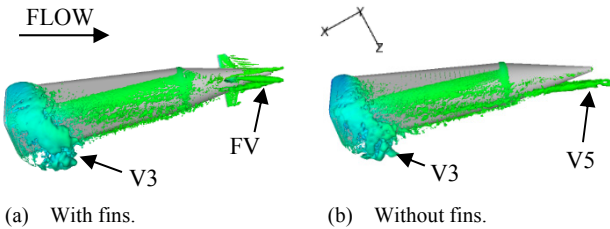

(a) With fins. (b) Without fins.

Fig. 18. Q isosurface colored with C_P (AOA=170 degrees).

Cp(pres.coef.): -1.4 -0.7 0 0.7 1.4
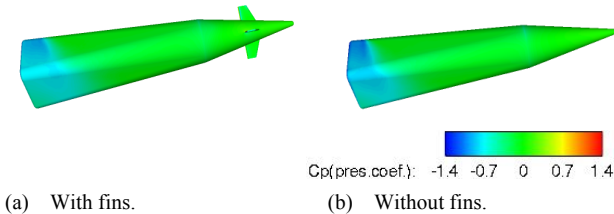
(a) With fins. (b) Without fins.

Fig. 19. Pressure distribution (AOA=170 degrees).

To summarize, the results at backward angles: as with forward angles, vortices are generated downstream of the fins.

However, the influence of these vortices on the downstream flow has a negligible effect on the pitching moment coefficients since the fins are installed on the nose (which is on the downstream side at backward angles). Only vortices near the body surface of the fins cause the increase in the pitching moment coefficients at backward angles.

4. Conclusions

In this study, we numerically simulated the flow around a reusable rocket on which fins are installed, obtained aerodynamic coefficients, and visualized flowfields. Our results are summarized as follows:

➢ Pitching moment coefficients can be increased by installing fins on the nose section (this result is in agreement with that of reference experiments).

➢ At AOAs of less than 90 degrees, fins (located upstream portion) caused the formation of vortices, and these vortices significantly affected the flowfields downstream. This resulted in an increase in pitching moment coefficients (+17-54 %).

➢ At AOAs of more than 90 degrees, vortices were also generated downstream of fins. However, the effect of the change in flowfields due to these vortices on the pitching moment coefficients was not as significant, as the fins were installed on the downstream side at these angles. Only vortices formed near the body surfaces of the fins affected the pitching moment coefficients in these cases (+43-81 %).

We have clarified the effect of flowfields on the pitching moment coefficients of a reusable rocket as described above. In future work, we plan to change the incidence angles of the fins and propose more suitable reusable rocket flight configurations. Also, we plan to conduct PIV experiments. We will compare the visualization results with our numerical results to verify the vortical flow structures.

Appendices

A. Effects of grid resolution

We generated a grid (designated as a fine grid) having almost twice as many nodes as the original (medium) grid to verify that our simulation produces grid-independent flowfield and pitching moment coefficient results. Due to cost limitations, it is difficult to conduct grid dependency studies at every AOA. Thus, we selected an AOA of 20 degrees as a representative case. Table 2 indicates that nearly identical results are acquired from fine and medium grids (the error is approximately 1.8%). In addition, Fig. 20 shows that the computed flowfield obtained from the fine grid is in agreement with that of medium grid. Therefore, it is confirmed that the flow structure can be well resolved using the original grid.

Table 2. Grid sensitivity test.

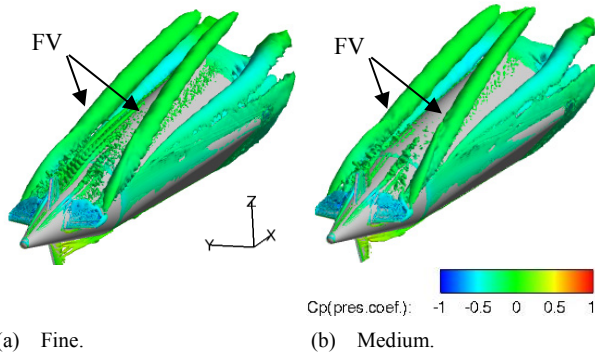| Grid	Number of nodes	Cm
Fine	55.09 million	0.167
Medium	28.70 million	0.164

(a) Fine.　　　　　　　(b) Medium.

Fig. 20.　Q isosurface colored with C_P (AOA=20 degrees).

B.　Results of RANS simulation

We conducted a RANS simulation as well as the DDES. SA-noft2[17] was adopted as the turbulence model, and other computational methods, conditions, and the grid were identical to those of the DDES. We selected an AOA of 60 degrees as a representative case. The Q isosurface acquired from the RANS simulation at this angle is shown in Fig. 21. In Fig. 21, fin-vortices (FV) and vortices (V2) can be observed, yet these vortices are symmetrical unlike in the case of the DDES shown in Fig. 12 (a). From this result, we determined that DDES is more capable of predicting the unsteady separated flow in comparison to a RANS simulation. Therefore, DDES would be ideal for use in this study.
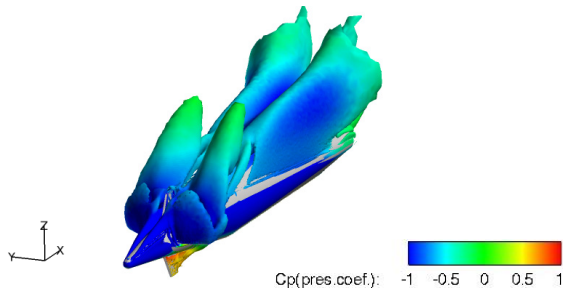

Fig. 21.　Q isosurface obtained from RANS simulation.

Acknowledgments

References

1) Inatani, Y., Naruo, Y., and Yonemoto, K.: Concept and Preliminary Flight Testing of a Fully Reusable Rocket Vehicle, *J. Spacecraft and Rockets*, **38** (2001), pp. 36-42.
2) Nonaka, S., Ogawa, H., and Inatani, Y.: Aerodynamic Design Considerations in Vertical Landing Rocket Vehicle, AIAA Paper 2001-1898, 2001.
3) Okamoto, Y.: Study on Turnover Maneuver of Reusable Rocket from Gliding to Vertical Landing, Master's Thesis, The University of Tokyo, 2014 (in Japanese).
4) Nonaka, S., Imamura, Y., Shimotashiro, S., Ogawa, H., and Intani, Y.: Turnover Maneuver of Vertical Landing Rocket Vehicle, 26th International Symposium on Space Technology and Science, Hamamatsu, 2008-g-20, 2008.
5) Shimojima, Y.: Study on Aerodynamic Characteristic of VTOL Rocket on Turn-Over Maneuver, Graduation Thesis, Tokyo University of Agriculture and Technology, 2016 (in Japanese).
6) Kinami, T.: Aerodynamic Characteristics of Slender Bodies at Turnover, Graduation Thesis, Yokohama National University, 2016 (in Japanese).
7) Aogaki, T., Kitamura. K., and Nonaka. S.: Computational Study of Aerodynamic Characteristics of Reusable Rocket at High-Angle-of-Attack, AIAA Paper 2017-1212, 2017.
8) Nakamura, M., Nonaka, S., and Inatani, H.: Aerodynamics of Reusable VTOL Rocket in Return Flight, JSASS-2014-4186, 2014 (in Japanese).
9) Hashimoto, A., Murakami, K., Aoyama, T., Ishiko, K., Hishida, M., Sakashita, M., and Lahur, P.: Toward the Fastest Unstructured CFD Code "FaSTAR", AIAA Paper 2012-1075, 2012.
10) Spalart, P. R., Deck, S., Shur, M. L., Squires, K. D., Strelets, M. Kh., and Travin, A.: A New Version of Detached-Eddy Simulation, Resistant to Ambiguous Grid Densities, *Theoretical and Computational Fluid Dynamics*, **20** (2006), pp. 181-195.
11) Shima, E. and Kitamura, K.: Parameter-Free Simple Low-Dissipation AUSM-Family Scheme for All Speeds, *AIAA J.*, **49** (2011), pp.1963-1709.
12) Shima, E., Kitamura, K., and Haga, T.: Green-Gauss/Weighted-Least-Squares Hybrid Gradient Reconstruction for Arbitrary Polyhedra Unstructured Grids, *AIAA J.*, **51** (2013), pp. 2740-2747.
13) Burg, C. O. E.: Higher Order Variable Extrapolation for Unstructured Finite Volume RANS Flow Solvers, AIAA Paper 2005-4999, 2005.
14) Venkatakrishnan, V.: Convergence to Steady State Solutions of the Euler Equations on Unstructured Grids with Limiters, *J. Computational Physics*, **118** (1995), pp. 120-130.
15) Kitamura, K., Shima, E., Fujimoto, K., and Wang, Z. J.: Performance of Low-Dissipation Euler Fluxes and Preconditioned LU-SGS at Low Speeds, *Communications in Computational Physics*, **10** (2011), pp. 90-119.
16) Ito, Y. and Nakahashi, K.: Direct Surface Triangulation Using Stereolithography Data, *AIAA J.*, **40** (2002), pp. 490-496.
17) Spalart, P. R., Allmaras, S.: A One-Equation Turbulence Model for Aerodynamic Flows, AIAA Paper 1992-439, 1992.